Enhancement of array processing techniques for CAA-based acoustic imaging

Simon Bouley, Joannès Chambon, Olivier Minck

Enhancement of array processing techniques for CAA-based acoustic imaging

Simon Bouley*, Joannès Chambon† and Olivier Minck‡
MicrodB, F-69134, Écully, France

Acoustic imaging techniques aim at retrieving equivalent sources on radiating devices from microphone signals. Widely used in wind tunnel, they allow to localize acoustic hot spots, estimate their acoustic power and directivity. Recent years have also seen several applications of array processing techniques on CAA (computational aeroacoustics) data, where the acoustic propagation is simulated on a set of virtual microphones. Avoiding installation effects and measurement noise, this process allows to multiply and test digital mock-ups before final experimental validation. By taking advantage of state-of-the-art phased-array techniques, this paper aims at defining a consistent strategy to perform three-dimensional numerical acoustic imaging. It therefore pays a specific attention to the modelisation of aeroacoustic sources, diffraction effects brought by three-dimensional transfer functions and the reconstruction of source correlation with inverse techniques. The strategy performances (source localization, quantification, directivity) are assessed against the LAGOON landing gear benchmark.

I. Introduction

In many industries, the ever-increasing computing capabilities available in research and development departments redefine the balance between physical testing and simulation, leading to a reorganization of product design cycles. The deep-set trend to reduce physical testing costs and its cumbersome procedures reinforces the role of simulation in the conception and validation of digital mock-ups. This model based development thus aims at reducing the number of physical prototypes while increasing product variants at the preliminary design stages, when the ease of conception change is maximal. This primary standpoint begins to be relevant in the domain of aeroacoustic-oriented conception in automotive or aeronautic industries. Many testing campaigns are carried out in wind tunnels for final comparison between optimized designs and for validation of almost market-ready products. Wind tunnel facilities dedicated to aeroacoustic studies typically gather hundreds of microphones located on the top and sides of the product (cars, aircraft's wing mock-up, landing gear...), itself immersed in a low Mach number flow [1]. Classical acoustic imaging techniques are then implemented to extract equivalent sources on the skin of the tested device, able to explain its acoustic radiation, and to draw acoustic maps. However, in addition to the high costs of facility rental charges, the results of these analysis must be weighed against irreducible installation effects or any kind of model bias. On the other side, the accuracy and the maturity of computational aeroacoustics (CAA) solvers and softwares make them accessible for engineers. In this respect, simulation-based analyses driven by acoustic imaging tools begin to be reachable. In a wind tunnel, acoustic pressure radiated around the immersed object is collected by a large set of microphones whose positions are compelled to fulfill technical specifications. For its part, numerical acoustic imaging involves a virtual array of microphones set as sensors in CAA solvers to gather acoustic propagation and performs array processing techniques to draw acoustic maps, cleared of any installation effects. The ability to overcome constraints on microphones position affords access to more accurate results in terms of both sound source localization and quantification, especially when three-dimensional scattering effects are significant.

In the past ten years, several studies illustrated the connection between CAA and acoustic imaging techniques, and the asset the latter can bring to aeroacoustic analysis. To get acoustic pressure on virtual array of microphones, some naturally derive a hybrid method combining computational fluid dynamics (CFD) solvers and aeroacoustic analogies (Lockard et al. [2] for instance), whereas others take benefit from compressible solvers to bring the array of sensors in the direct sound computation region and compute the acoustic perturbations without any intermediate step (see Pignier et al. [3]). This acoustic field is then combined with classical phased-array techniques to recover the sources. Hence, a

*R & T engineer (PhD), simon.bouley@microdb.fr.
†R & T engineer (PhD), joannes.chambon@microdb.fr.
‡R & T team leader, olivier.minck@microdb.fr.

great deal of effort has been led to improve the solvers ability to accurately simulate the acoustic field captured by virtual arrays. On its side, the acoustic imaging community keeps on completing their inverse methods, taking into account more and more properties of the equivalent sources and their propagation. State-of-art algorithms showed their effectiveness to deal with correlated sets of equivalent sources [4], three-dimensional volumetric source localization ([5], [6], [7]), dipolar-based equivalent sources ([8], [9], [10], [11]), or complex transfer functions around diffracting bodies ([12], [13]).

Therefore, this study aims at gathering some of these advances into a consistent numerical acoustic imaging process, dedicated to computational aeroacoustic analysis. The paper is organized as follows. Section II briefly reviews the literature about numerical acoustic imaging techniques. Section III makes use of aeroacoustic analogies to define properties of the equivalent sources. Section IV describes the calculation of both monopolar and dipolar transfer functions in presence of diffracting bodies. Section V discusses the ability of inverse methods to recover correlation between equivalent sources and Sec. VI assesses the proposed method against the LAGOON landing gear benchmark.

II. Numerical acoustic imaging

The simulation of far field flow-induced noise is often based on aeroacoustic analogies : the steady and unsteady properties of the flow are computed in the vicinity of the immersed object of study, then near-field CFD solution is propagated in the far field with integral formulations. To do so, hybrid methods split the acoustic generation carried out with LES/DES (Large/Detached Eddy Simulation) from far field acoustic propagation using Ffowcs-Williams and Hawkings analogy (FW-H [14]), especially to simulate the acoustic pressure at a reference microphone and to compare computed and experimental data. These past ten years, several studies added to this process a new stage dedicated to acoustic imaging : the acoustic pressure field is computed on a virtual array of microphones outside the unsteady flow region then microphone pressures are back-propagated in the vicinity of the object to retrieve an equivalent source distribution in the unsteady flow region ([15], [16], [17], [18], [19], [20], [21]). For instance, Lockard et al. [2] employed this methodology to compare simulated and experimental data. On one hand, a numerical semispan aircraft model is studied with the help of a hybrid Reynolds-Averaged-Navier-Stokes (RANS) / Large-Eddy-Simulation (LES) solver associated with a FW-H propagation code. On the other hand, a physical twin model has been studied in the same geometrical configuration. Then, classical acoustic imaging techniques such as Conventional Beamforming (CBF) and deconvolution methods, DAMAS [22] and CLEAN-SC [23], have been applied on both datasets to perform comparisons. These methods rely on uncorrelated distribution of monopolar sources, located on the nodes of a bidimensional calculation grid. According to the authors, the lack of wind-tunnel installation effects and experimental background noise entails a significant improvement of the acoustic imaging results : synthetic acoustic maps seem to be cleaner and less sensitive than experimental ones. Even if CFD results are of primary interest to study the underlying noise generation mechanisms, acoustic maps tend to bring new ways to assess low-noise conception, in terms of frequency range, localization and quantification.

However, the final result of this hybrid method largely depends on the quality of the FW-H propagation, which can contains bias errors, such as the choice of the surface control or the acoustic propagation model. To fix this, some authors suggest to directly locate virtual microphones in the direct sound computation region of compressible solvers (outside unsteady flow region) to evaluate acoustic perturbations ([24], [25]), short-circuiting aeroacoustic analogies. To this end, Pignier et al. [3] proposed a direct numerical beamforming (DNB) combining a RANS simulation and a compressible Improved Delayed DES (IDDES) computation to directly simulate the acoustic signals captured by a bidimensional virtual array in the steady region of the flow. As acoustic imaging assumptions, authors considered a bidimensional grid of monopoles, with a free-field propagation condition. Both a Moore-Penrose pseudo-inverse and a deconvoluted beamforming methods are used to perform back-propagation. The pseudo-inversion is able to recover correlation between sources, but is strongly subject to instability and conditioning issues. Authors took advantage of truncated singular value decomposition (TSVD) to regularize the inverse problem. To deconvolute beamforming maps, authors derived a dual-linear programming (LP) beamforming approach from Dougherty et al. [26]. The main idea behind this DNB technique is to provide an equivalent source distribution whose acoustic radiation mimics the one from the aerodynamic interaction between the flow and the object. To assess their method, a FW-H analogy is employed to compute the acoustic far field at a reference virtual microphone, outside the direct sound computation region, and is compared to the propagation of sources obtained with DNB method. This global approach has been applied to a submerged air inlet, and comparisons showed a good agreement between spectra computed by both FW-H analogy and DNB, whereas pseudo-inversion fails to reproduce accurate source location. Nevertheless, authors

pointed out some assumptions that could limit the analysis. Although DNB is more robust than pseudo-inversion, it cannot model correlation between sources, responsible of a large part of source directivity. Monopolar radiation of reconstructed source distribution can be queried in regards of the FW-H analogy, decomposing aeroacoustic sources as sets of monopoles, dipoles and quadrupoles. The free-field propagation hypothesis can be valid when the source grid is a bidimensional projection plane outside the radiating object, but ceases to be accurate in three-dimensional geometries where diffraction effects begin to be significant. Also, using a three-dimensional array of virtual microphones surrounding the object of study would increase both the performances of the array and the accuracy of the acoustic maps.

As a consequence, this study takes place in the wake of the cited papers and aims at bringing the deployed acoustic imaging technique to the state of the art. The global strategy is defined as follows. A classical hybrid methodology combining CFD near-field solutions and a far field propagation analogy (FW-H, Curle [27], Kirchhoff integral [28] or APE [29]) or a compressible simulation (Lattice Boltzmann method [30]) is used to compute acoustic pressure field at a three-dimensional virtual microphone array position, designed to completely surround the object of study. To take source correlation into account, the proposed array processing technique relies on a probabilistic inverse method denoted as Bayesian focusing [4], which proved its ability to correctly reconstruct correlated source distributions in terms of localization, quantification and directivity for larger frequency range than classical methods. Aeroacoustic analogies such as solid FW-H formulation have defined a sound source typology declined in three source sets : monopolar and dipolar surfacic distributions and a quadrupolar volumic distribution. Often, the quadrupolar components are precluded as their computation is time-consuming and their effects are of second-order. As monopolar are a commonplace source model for acoustic imaging, a specific effort has been carried out to include dipolar equivalent source in the proposed method. Also, as the three-dimensional array of microphones surrounds the tested object, the calculation grid can be identified to its three-dimensional mesh (or a decimated one), where nodes are considered as equivalent sources. This allows to directly back-propagate the acoustic field on the object and not on a bidimensional projection plane. Contrary to the latter, this three-dimensional configuration leads to consequential diffraction effects on the acoustic propagation, namely on transfer functions between source nodes and virtual microphones. As a consequence, a specific dipolar equivalent source method (ESM) is proposed to compute monopolar or dipolar source radiation and scattering transfer functions at once.

III. Aeroacoustic source model and propagation

This section aims at defining the far field acoustic propagation from CFD solutions in the vicinity of the tested object to the virtual microphones, with the help of aeroacoustic analogies. A keen interest is paid on the physical interpretation of aeroacoustic source distribution in the FW-H formulation, to define at best the acoustic imaging equivalent sources.

A. FW-H source terms

The classical FW-H equation defines a reorganization of continuity and Navier-Stokes equations in presence of variables jump brought by a discontinuity surface in arbitrary motion, denoted as data surface $f(\mathbf{x}, t)$, that could coincide with the solid surface of the tested object (solid condition) or not (permeable condition). The solid FW-H equation reads [31] :

$$\Box p(\mathbf{x}, t) = \frac{\partial}{\partial t}\{\rho_0 v_n \delta(f)\} - \frac{\partial}{\partial x_i}\{\ell_i \delta(f)\} + \frac{\partial^2}{\partial x_i \partial x_j}[T_{ij} H(f)], \tag{1}$$

where $\Box$ is the d'Alembert (wave) operator, p the acoustic pressure, $\mathbf{x}$ the observer position and ρ_0 the quiet medium density. v_n is the local normal ($\mathbf{n}$) velocity of the data surface, $\delta(f)$ a Dirac delta function, ℓ_i represents the local force intensity components that act on the fluid, T_{ij} the Lighthill stress tensor and $H(f)$ a Heaviside function.

The two first source terms are mathematically defined as surface sources and represent monopolar (thickness) and dipolar (loading) sources distribution on the data surface $f = 0$, whereas the third term represents the volumic quadrupolar sources outside the data surface. Nevertheless, some features limit this interpretation. First, separation of sources terms in monopolar, dipolar and quadrupolar distribution is not valid anymore when the data and the solid surfaces do not coincide. This equation assumes (with the Heaviside function) that the quadrupolar sources are outside the data surface while all physical sources surrounded by the data surface contribute to the surface terms. Therefore, if a permeable surface is able to contain all physical sources inside it, the volumic source distribution becomes negligible.

This strategy allows then to remove the time-consuming computation of the Lighthill stress tensor in the whole volumic domain. However, as all sources are expressed by surface distributions, no physical source identification to monopolar, dipolar and quadrupolar distribution can be done anymore. Second, this mathematical interpretation is not unique. Isom [32] and then Farassat ([33], [34]) proved the equivalence between the thickness noise and a uniform loading noise of source strength $\rho_0 c^2$, and can therefore be derived as a dipolar source distribution. Finally, a great care must be taken to analyse these distributions behaviour when the object is moving as they cannot be seen as stationary sources. Doppler frequency shift as well as Doppler amplification due to source motion must be considered.

Usually, only surfacic source distributions are computed, due to the computational cost of volumic sources, themselves considered negligible according to energetic analysis. For instance, in their paper on non-linear interactions in gas, Chu and Kovásznay [35] demonstrated that the three modes of gas oscillation (sound, vorticity and entropy) generate non-linear and linear interactions when they are coupled by solid boundaries or gradients. They also concluded that all sound generation mechanisms are not of same order of magnitude. More specifically, aeroacoustic sound generated by the linear acoustic-vorticity coupling at physical boundaries overwhelms sound generated by the non-linear self-interaction of the turbulence itself. In other words, FW-H surfacic source distributions are at least one order of magnitude higher than volumic sources. However, as stated by Hajczak et al. [36], the assumption of compactness of the aeroacoustic sources may tend to misunderstood the effective balance between surfacic and volumic sources radiation, especially at high frequencies. For example, the acoustic radiation of vortex shedding induced by an immersed cylinder can be view as the propagation of volumic quadripolar sources diffracted by the cylinder (Curle's analogy), or the radiation of surfacic dipolar sources on the cylinder (FW-H analogy), as long as the cylinder section is acoustically compact. The compactness of a source can be analysed in relation to Helmholtz number, defined as the characteristic length divided by acoustic wavelength, or as the multiplication of Mach and Strouhal numbers. Therefore, for low-Mach number flow, the compactness can be assumed valid, but may be not for high frequencies, as well as the analogies equivalence. With the help of numerical acoustic imaging, authors showed that in non-compact conditions (at high frequencies), quadrupolar sources downstream an immersed object tend to dominate dipolar sources, whereas they do not at lower frequencies. Therefore, as long as the sources remain compact, the quadrupolar source distribution can be neglected, but a special care must be taken when the frequency range exceeds the compactness limitations.

B. Wind Tunnel formulation

The FW-H solution, as well as formulations 1 and 1A derived by Farassat ([37], [38]), describes acoustic wave propagation of arbitrary moving surfaces in a quiescent medium with a fixed observer in the chosen reference frame. As illustrated by Weckmüller et al. [39], this configuration is not well-suited to wind-tunnel application (or its digital twin), where the medium is moving and the immersed object is not. Ways to correctly implement the latter configuration imply either to move the observer at the same speed as the moving engine, or to embed a fixed object in a moving medium. Wells and Han [40] first derived a convective FW-H equation for the moving-observer problem. Najafi-Yazdi et al. [41] derived a convective FW-H solution denoted as formulation 1C dedicated to simulate wind-tunnel acoustic measurements of stationary or moving sources in presence of a uniform mean flow. A specific *wind tunnel* formulation is expressed when both source and observer are stationary. Neglecting the quadrupolar source, simplified thickness (p_T) and loading noise (p_L) terms are then derived :

$$4\pi p_T = \int_{f=0} \left[(1 - M_0) \frac{\dot{Q}_i n_i}{R^*} - U_0 \frac{\tilde{R}_1^* Q_i n_i}{R^{*2}} \right]_{\tau_e} \mathrm{d}\eta, \tag{2}$$

$$4\pi p_L = \int_{f=0} \left[\frac{1}{c_0} \frac{\dot{L}_{ij} n_j \tilde{R}_i}{R^*} + \frac{L_{ij} n_j \tilde{R}_i^*}{R^{*2}} \right]_{\tau_e} \mathrm{d}\eta, \tag{3}$$

where Q_i and L_{ij} refer to convective thickness and loading source terms including mean flow velocity, while $[]_{\tau_e}$ denotes integrand evaluation at the emission time τ_e and η the surface of integration. U_0 and M_0 are the flow speed and Mach number, respectively and R variables express various distances.

IV. Transfer functions for acoustic imaging around diffracting bodies

A. Source model

The underlying aim of acoustic imaging technique is to reconstruct a source distribution able to reproduce the acoustic directivity measured by the microphone array. In that respect, we do not look for the true amplitude of FW-H surfacic sources (as proposed by Evans et al. [10] for instance), but tend to find an equivalent set of sources that reflects the behaviour of the aeroacoustic propagation from the sources toward the microphones.

The success of array processing lies in the accurate resolution of the classical inverse problem

$$\mathbf{p} = \mathbf{H}\mathbf{q} \tag{4}$$

between measured or simulated acoustic pressures $\mathbf{p}$ and sources $\mathbf{q}$ distributed on a localization grid, linked by Frequency Response Functions (FRF) gathered in the matrix $\mathbf{H}$. This acoustic imaging inverse problem relies on two cornerstones : the choice of the propagation model and the inversion techniques. This section deals with the first one whereas the latter is addressed in Sec. V. Naturally, the choice of the propagation model drives the nature of the reconstructed sources. Monopolar sources in a free-field medium constitute the most widespread model due to its versatility and its robustness (see [42] or [43] for in-depth analysis). However, aeroacoustic analogies, as seen in the previous section, tend to mainly describe surfacic sound sources as dipolar. Because of its lack of directivity, array processing based on monopolar models applied to aeroacoustic sources in a three-dimensional configuration may fail to accurately localize them. Accordingly, authors introduced free-field dipolar transfer functions in acoustic imaging ([44], [8]) and extended these approaches in three-dimensional domains ([9], [11]). This paper assumes to mainly reconstruct sources on surfaces, either planar surfaces within cross-sections of the body, or directly on its skin. Volumic array processing (such as [5]) may allow to reconstruct quadrupolar sources distribution around the radiating body, but for low-Mach number flow, quadrupolar noise remains negligible. Hence, this aspect is not addressed at this stage of the study, but remains a significant subject of investigation.

Acoustic imaging is based on phase relationships : they act as a significant factor in both the transfer functions between potential sources and microphones and the correlation between the sources themselves. As explained previously, integration of three-dimensional features needs a specific care of diffraction effects around the radiating body. Whereas free-field FRFs can be adequate when both the calculation and measurement grids are planar and face each other, they cease to be when the geometrical complexity increases. Therefore, the following sections aim at defining a process to compute monopolar or dipolar FRFs while taking into account the diffraction effects brought by the radiating body itself.

B. Equivalent Source Method for FRF computation

Various ways exist to compute FRFs. Transfer functions can be calculated analytically but are limited to simplest shapes (cylinder, sphere, reflecting planes). Alternatives are either time-consuming (Boundary Element Method (BEM) or Finite Element Method (FEM)) or not feasible in practice (measured transfer functions, see [45]). To compete with BEM, alternative technique denoted as Equivalent Source Method (ESM) was developed for the simulation of acoustic waves scattered by rigid bodies ([46], [47]). Thanks to the reciprocity principle ([48], [49], [50]), a slight derivation of this direct technique of acoustic propagation has been proposed to compute FRFs upstream of the imaging process. The reciprocity principle (or Rayleigh reciprocity theorem [51]) denotes an equivalence between acoustic radiation from one point to another and vice versa. In terms of Green's function, this principle can be expressed as :

$$G(\mathbf{x}|\mathbf{x}_0, k) = G(\mathbf{x}_0|\mathbf{x}, k), \tag{5}$$

where $\mathbf{x}_0$ and $\mathbf{x}$ are point source and receiver, respectively, and k is the wave number. This principle is extensible to any multipoles such as dipoles or quadrupoles. Adapted to acoustic imaging, FRF can be defined for each frequency as the ratio between the pressure p_i^j induced at one microphone i by the volumic flow q_j at the grid node j. This ratio includes any acoustic propagation features (diffraction, refraction or reflection effects). The reprocity principle indicates that FRF can be understood as the ratio between the volumic flow of a source placed on a microphone position and the pressure taken on the grid node. Instead of computing the direct propagation of acoustic sources located on the object toward microphones, while taking diffraction effects into account, the reciprocal strategy leads to compute the total

acoustic field (incident and diffracted) received on the object when a source located at one microphone is radiating. ESM is therefore used to determine the diffracted field.

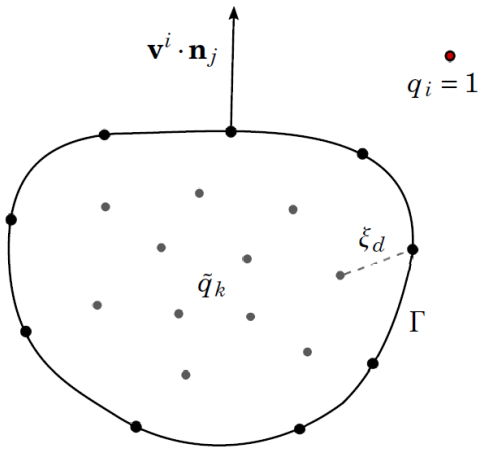

Figure 1 A synthesized depiction of ESM [52]. A q_i unitary source located at one microphone position radiates an incident acoustic field on the diffracting body, whose skin Γ is discretized in N nodes. $\tilde{q}_k$ equivalent sources to find allow to counter balance the normal velocity on Γ induced by q_i.

In a nutshell, ESM can be synthesized as followed : let consider a scattering object defined by its boundary Γ and a homogeneous Neumann boundary condition on its discretized skin of N nodes. N_s artificial sources of volumic flows $(\tilde{q}_k)_{k\leq N_s}$ are located inside Γ. ESM aims at tuning this set of sources to meet the boundary conditions that mimic the real diffraction effect of the rigid body. In a word, these *equivalent sources* are adjusted to counter balance the normal velocity $\mathbf{v}^i \cdot \mathbf{n}_j$ induced by a unitary radiating source q_i (located at one microphone position) at every nodes on Γ (Fig. 1). This equivalence was first stated by Koopman et al. [53] and is based on the well-posedness of the Helmholtz problem under boundary conditions. If so, the pressure field outside Γ is a linear combination of fundamental solutions, fulfilling boundary conditions. Mathematically, the ESM problem boils down to find the equivalent sources $\tilde{\mathbf{q}}^i \in \mathbb{C}^{N_s}$ such that

$$\mathbf{v}^i \cdot \mathbf{n}_j = -\nabla\mathbf{G}\tilde{\mathbf{q}}^i, \tag{6}$$

where $\nabla\mathbf{G}$ expresses the free field transfer between equivalent sources volumic flows and their normal velocities on the boundary Γ. Equation (6) expresses an equivalence between velocities on Γ induced by both equivalent sources and the incident field. The global strategy can therefore be summed up in three steps :

1) Calculate the normal velocity radiated by a unitary source on every grid node, representing the incident velocity equivalent sources must offset.
2) Inverse Eq. (6) to find complex amplitude of equivalent sources $\tilde{\mathbf{q}}^i$.
3) Back-propagate both incident ($\mathbf{D}_{ij}$) and diffracted acoustic fields on skin nodes to define complete FRF :

$$\mathbf{H}_{ij} = \mathbf{D}_{ij} + \mathbf{G}\tilde{\mathbf{q}}^{ij}. \tag{7}$$

This strategy has been derived for both monopolar [52] and dipolar [12] sources, whose mathematical developments are briefly synthesized in the following sections.

C. Monopolar ESM

The monopolar transfer function between a volumic flow q_j and acoustic pressure p^i_j defines the classical free field FRF :

$$\mathbf{D}_{ij} = -\mathrm{i}\omega\rho_0 \frac{\mathrm{e}^{\mathrm{i}kr_{ij}}}{4\pi r_{ij}}, \tag{8}$$

where ω is the angular frequency and r_{ij} the distance between a node and a microphone. The first step is to compute the left side of Eq. (6). Let θ_{ij} be the angle between $\mathbf{r}_{ij}$ and the normal $\mathbf{n}_j$ to Γ at the j^{th} node (also denoted as control point):

$$\mathbf{v}^i \cdot \mathbf{n}_j = \frac{\mathrm{e}^{\mathrm{i}kr_{ij}}}{4\pi r_{ij}^2} \left(1 - \mathrm{i}kr_{ij}\right) \cos\theta_{ij}. \tag{9}$$

The right side of Eq. (6) involves the computation of $\nabla\mathbf{G}$ between equivalent sources and control points :

$$\nabla\mathbf{G}_{jk} = \frac{\mathrm{e}^{\mathrm{i}kr_{jk}}}{4\pi r_{jk}^2} \left(1 - \mathrm{i}kr_{jk}\right) \cos\theta_{jk}. \tag{10}$$

Once Eq. (6) is solved for all unitary sources, the equivalent sources are propagated towards control points and added to the incident field to determine the total FRF. Chambon et al. [52] also derived transfer functions involving ground reflection and shear layer refraction, according to Amiet's model [54], these being major installation effects in wind tunnel facilities.

D. Dipolar ESM

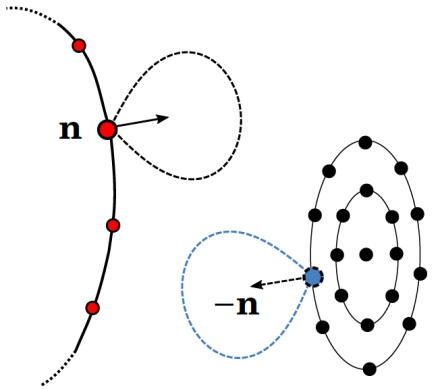

Figure 2 Reciprocity principle applied to dipolar FRFs [12]. The computation of a half dipole on the mesh radiating toward a microphone can be traded against the one of a dipole with opposite direction located on the array toward the surface.

Chambon et al. [12] also derived an Equivalent Source Method dedicated to dipolar sources (Fig. 2). Evans et al. [10] developed an acoustic imaging technique able to reconstruct loading noise issued from immersed body in low-Mach number flows. They therefore defined a half dipole formulation that radiates only outside the body :

$$D_{ij} = \begin{cases} A_j \frac{\mathrm{e}^{\mathrm{i}kr_{ij}}}{4\pi r_{ij}^2} \left(1 - \mathrm{i}kr_{ij}\right) \mathbf{r}_{ij} \cdot \mathbf{n}_j & \text{if} \quad \mathbf{r}_{ij} \cdot \mathbf{n}_j > 0, \\ 0 & \text{if} \quad \mathbf{r}_{ij} \cdot \mathbf{n}_j < 0. \end{cases} \tag{11}$$

A_j denotes the surface of the j^{th} element of the mesh. First, the normal velocity at control points due to the acoustic incident field reads :

$$\mathbf{v}_\alpha^{ij} = A_j \frac{\mathrm{e}^{\mathrm{i}kr_{i\alpha}}}{4\pi r_{i\alpha}^3} \begin{bmatrix} (k^2 r_{i\alpha}^2 - 2\mathrm{i}kr_{i\alpha} + 2)\mathbf{r}_{ij} \cdot \mathbf{n}_j \\ \mathrm{i}kr_{i\alpha} + 1 \end{bmatrix} \cdot \mathbf{n}_\alpha, \quad \forall\alpha \leq N. \tag{12}$$

Second, the equivalent monopoles inside Γ are calibrated :

$$\tilde{\mathbf{q}}^i = \nabla\mathbf{G}^+\mathbf{v}^i, \tag{13}$$

where $\nabla\mathbf{G}^+$ is the pseudo-inverse of Eq. (10). Finally, the total FRF $\mathbf{H}$ is computed the same way as for monopolar ESM. This provides a FRF between dipoles on the microphones array and nodes on the mesh. In accordance with the reciprocity principle, the Hermitian conjugate of the obtained $\mathbf{H}$ matrix allows to recover FRF between dipoles on nodes and microphones. Note that the computational cost is increased for dipolar ESM, as a loop on each node is needed to integrate the variation of dipole normal vectors in the computation of the incident velocity field. Additional details about stability and computational costs can be found in [12].

V. Inverse techniques

The resolution of Eq. (4) involves an accurate propagation model and an efficient inversion technique. The first was detailed in the previous section whereas the latter is studied in this one. As listed in literature reviews by Leclère *et al* [55] and Merino-Martínez et al. [56], many array processing techniques were developed to recover acoustic sources from microphone signals. Three of them are briefly detailed in this section : Conventional Beamforming (CBF [57]), CLEAN-SC [23] and Bayesian Focusing (BF, [58], [4]). The first two methods are identified as *beamforming-type*: they aim at solving a scalar inverse problem, where the amplitude of each source is computed independently from the others. Contrariwise, Bayesian Focusing considers a matrix inverse problem where sources are obtained all at once, taking sources interferences into account. Bearing in minds that CBF is a standard method taken as reference, comparisons between these three techniques will highlight their ability to estimate the accurate source distribution on three-dimensional configurations as well as far field acoustic spectrum. All algorithms are formulated in frequency domain, and the inverse problem is then independently solved for each frequency bin.

A. CBF

Conventional Beamforming is the most widespread array processing technique because of its algorithmic simplicity, its computational efficiency and its robustness against noise and model bias. Adapted for quadratic variables, Eq. (4) is rewritten as a least squares problem for each node of the calculation grid :

$$|\tilde{q}_j|^2 = \text{argmin} \, \|\mathbf{S}_{\text{pp}} - |q_j|^2 \mathbf{H}_{:,j}\mathbf{H}_{:,j}^H\|_F^2, \tag{14}$$

where $\mathbf{S}_{\text{pp}} = \mathbf{p}\mathbf{p}^H$ is the cross-spectral matrix (CSM) of the measured pressure signals. This least squares resolution aims at minimizing the residue between measured CSM $\mathbf{S}_{\text{pp}}$ and the synthetic CSM $|q_j|^2\mathbf{H}_{:,j}\mathbf{H}_{:,j}^H$ generated by a single source located at the focus node j of squared amplitude $|q_j|^2$ with a transfer function to each microphones $\mathbf{H}_{:,j}$, where the latter is the j^{th} column of FRF $\mathbf{H}$. The solution reads :

$$|\tilde{q}_j|^2 = \frac{\mathbf{H}_{:,j}^H\mathbf{S}_{\text{pp}}\mathbf{H}_{:,j}}{\|\mathbf{H}_{:,j}\|^4}. \tag{15}$$

From Eq. (15), it clearly appears that CBF is a point-to-point process as amplitudes are successively computed for each focus node independently of its neighbours. The consequence is twofold. First, energy leakage occurs from one node to its neighbours resulting in the presence of lobes. When several sources are radiating, CBF fails at accurately recover strengths of any of the sources. The attenuation of this leakage, seen as the array footprint on acoustic maps, is the main goal of deconvolution techniques as CLEAN-SC, presented in Sec. (V.B). Second, correlation between sources cannot be retrieved whereas source phase relationships play a crucial role in the directivity pattern. Significant discrepancies are then expected in power estimation and far field repropagation when CBF is employed.

B. CLEAN-SC

As mentioned in the previous section, CBF actually carries out a spatial convolution between the acoustic field and the microphone array. This footprint is denoted as Point Spread Function (PSF), whose pattern is mainly driven by the spatial arrangement of microphones and the frequency. Therefore, polluting artifacts occur in the resulting acoustic maps as main and side lobes. Among others, CLEAN-SC algorithm has become popular in the aeroacoustic imaging domain due to its robustness and cost effectiveness. The main goal of this algorithm is to remove iteratively from the measured CSM what is coherent to the beamforming map maximum (the beamforming map being considered as a *dirty*

map while the maximum is added to a *clean map*). This allows to remove lobes and then to drastically increase the dynamic between sources of highest and lowest amplitudes. The iterative algorithm is summed up in the following :

1) Initialization : Compute CBF acoustic map (the *dirty map*) and initialize a degraded CSM $\mathbf{D}^{(0)}$ by the measured one $\mathbf{S}_{\text{pp}}$.
2) Clean map update : Search for maximum peak position $\boldsymbol{\xi}_{\text{max}}^{(i+1)}$ in the dirty map and store its power $P_{\text{max}}^{(i+1)}$ at the same location.
3) CSM update :
    1) Compute the coherent steering vector $\mathbf{H}^{(i+1)}$ using the (degraded) CSM and the focused signal in $\boldsymbol{\xi}_{\text{max}}^{(i+1)}$.
    2) Compute the CSM $\mathbf{C}^{(i+1)}$ induced by the source in $\boldsymbol{\xi}_{\text{max}}^{(i+1)}$.
    3) Compute the degraded CSM $\mathbf{D}^{(i+1)} = \mathbf{D}^{(i)} - \mathbf{C}^{(i+1)}$.
    4) Loop until degraded CSM energy stops decreasing.

Deconvolution algorithms such as CLEAN-SC proved their ability to efficiently remove array processing artifacts. However, as CLEAN-SC is initialized with a beamforming map, the algorithm will not be able to separate two close sources merged as one, especially at low frequencies (HR-CLEAN-SC [59] aims at solving this limitation). Also, the algorithm only considers uncorrelated sources. If a set of sources are coherent or spatially extended, they will be considered as side lobes and will be removed. CLEAN-SC is therefore well-suited for any sparse uncorrelated ensemble of sources. Porteous et al. [9] showed both the efficiency and limits of CLEAN-SC to retrieve dipolar sources in a three-dimensional configuration.

C. Bayesian Focusing

To deal with source correlation, the calculation of only auto powers (diagonal terms of the source cross-spectral matrix) is not sufficient : off-diagonal terms need to be determined. To do so, point-to-point methods techniques must give way to inverse techniques. One naive inverse solution of Eq. (4) is to introduce Moore-Penrose pseudo-inverse of $\mathbf{H}$ to find estimate of the whole vector $\mathbf{q}$ at once, allowing to retrieve phases between sources. However, as the number of grid nodes is larger than the number of microphones, the inversion is under-determined leading to an infinite range of solutions. Also, pseudo-inversion is very sensitive to noise, yielding unstable results. In a nutshell, this problem is often ill-posed in the sense of Hadamard [60]. Regularization techniques, such as Tikhonov regularization [61] aim at minimize both the least squares residue and the norm of the solution by means of a regularization parameter λ. This updated formulation reads :

$$\tilde{\mathbf{q}} = \text{argmin}\|\mathbf{p} - \mathbf{H}\mathbf{q}\|^2 - \lambda^2\|\mathbf{q}\|_p^2, \tag{16}$$

or

$$\tilde{\mathbf{S}}_{qq} = \text{argmin}\|\mathbf{S}_{\text{pp}} - \mathbf{H}\mathbf{S}_{qq}\mathbf{H}^H\|_F^2 - \lambda^2\|\mathbf{S}_{qq}\|_p^2, \tag{17}$$

where $p \in [1, 2]$ is the value of the p-norm. Its influence on the regularization is discussed in Leclère et al. [55]. Automatic computation of λ were proposed as general cross validation (GCV [62]) or L-curve (see Hansen [63] for complete details). Also, the complete $\tilde{\mathbf{S}}_{qq} \in \mathbb{C}^{N\times N}$ is now computed, and not only its diagonal terms. A more robust algorithm to solve Eq. (16) has been proposed by Antoni [58] taking benefit from probabilistic framework and denoted as Bayesian Focusing (BF). Its underlying principles are resumed in short in this section. An extended description of the method has been presented by Pereira et al. [64].

In a word, Bayesian Focusing aims at reconstructing the most probable source distribution given a finite set of measurements. To do so, the unknown $\mathbf{q}$ is considered as a random variable, the goal being to determine its probability density function (PDF), based on information provided by the microphones signals, noted as $[\mathbf{q}|\mathbf{p}]$. Especially, the maximum of this *posterior* pdf indicates the most probable positions and amplitudes of the sources :

$$\tilde{\mathbf{q}} = \text{argmax}[\mathbf{q}|\mathbf{p}]. \tag{18}$$

According to Bayes rule, the posterior pdf can be calculated from a prior pdf $[\mathbf{q}]$ and a likelihood function $[\mathbf{p}|\mathbf{q}]$:

$$[\mathbf{q}|\mathbf{p}] = \frac{[\mathbf{p}|\mathbf{q}][\mathbf{q}]}{[\mathbf{p}]}. \tag{19}$$

The source prior defines *a priori* known information about the source distribution (covariance, mean, sparsity) while the likelihood function expresses the direct probability of the measured signals $\mathbf{p}$ given a propagation model and measurement noise. In general, these pdf are designed as Gaussian distributions :

$$[\mathbf{p}|\mathbf{q}]\,[\mathbf{q}] \sim \mathcal{N}(\mathbf{Hq}, \beta^2\mathbf{I}_M), \quad [\mathbf{q}] \sim \mathcal{N}(0, \alpha^2\mathbf{\Omega}_q), \tag{20}$$

where $\beta^2\mathbf{I}_M$ represents the energy of uncorrelated measurement noise, α^2 the *a priori* overall energy of the sources and $\mathbf{\Omega}_q$ the covariance matrix of the sources. The latter provides *prior* information about correlation between sources. With Gaussian priors, the result boils down to a Tikhonov solution :

$$\tilde{\mathbf{q}} = \text{argmin}(-\ln([\mathbf{p}|\mathbf{q}]\,[\mathbf{q}]) = \text{argmin}\{\|\mathbf{p} - \mathbf{Hq}\|_2^2 + \lambda^2\|\mathbf{\Omega}_q^{-1}\mathbf{q}\|_2^2\}, \quad \lambda^2 = \frac{\beta^2}{\alpha^2}. \tag{21}$$

The solution of this regularized least squares problem reads :

$$\tilde{\mathbf{q}} = \mathbf{\Omega}_q^{1/2}\mathbf{H}^H\mathbf{S}^{-1}\mathbf{U}\mathbf{H}\frac{\mathbf{S}}{\mathbf{S}^2 + \lambda^2}\mathbf{U}^H\mathbf{p}, \tag{22}$$

where $\mathbf{S}$ and $\mathbf{U}$ are diagonal and unitary matrices from the singular value decomposition (SVD)

$$\mathbf{H}\mathbf{\Omega}_q^{1/2} = \mathbf{USV}^H. \tag{23}$$

While the regularization parameter λ must be tuned in ancillary procedure in classical inverse techniques, Pereira et al. [64] proposed inner algorithms to compute it, clearly identified as a noise-to-signal ratio (ratio of expected noise energy β^2 to source energy α^2). Finally, Antoni et al. [4] derived an iterative Bayesian Focusing algorithm, able to modify spatial prior of the source $\mathbf{\Omega}_q$ to strengthen the resolution, especially in case of sparse sources, improving acoustic map reconstruction in terms of localization, quantification and directivity. This current state-of-the-art algorithm, designed as iterative Bayesian Focusing (iBF), encompasses under the same formalism several configurations in terms of correlation, sparsity and regularization strategies. Its ability to accurately estimate acoustic maps, source power or directivity pattern makes it a very powerful and versatile tool for acoustic imaging.

VI. Application on LAGOON benchmark

Many authors applied acoustic imaging techniques on numerical simulation of landing gear noise. For instance, Bouchouireb et al. [65] investigated the ability of the DNB algorithm (mentioned in Sec. II) to localize sources on a simulated landing gear and compare their repropagation in the far field to FW-H results. Rougier et al. [66] employed a hybrid method composed of LBM (lattice Boltzmann method) results and FW-H analogy to simulate acoustic pressure in the far field. This allowed them to separately propagate sources related to the different parts of the landing gear, in order to identify components that produce major sources of noise. They also make use of stereo-beamforming with a set of six planar arrays of microphones to estimate source location in a volumic space. Originally designed for a project funded by Airbus, the LAGOON (LAnding Gear NOise database for CAA validatiON) device is a simplified two-wheel landing gear including cylindrical leg and axle but without fuselage parts, well-suited to compare both numerical and experimental methods [67]. Bulté and Redonnet [68] studied the performances of array processing on this typical test case. The noise generation stage is performed with a ZDES (Zone Detached Eddy Simulation, solver elsA) while the propagation is carried out with a time domain structured CAA method (solver sAbrinA). Authors retropropagate both measured and simulated microphone signals on bidimensional cross-sectional planes around or within the landing gear with the help of CBF or DAMAS algorithms. Comparisons of results obtained with both experimental or simulated datasets showed the effectiveness of the numerical strategy, avoiding installation effects, leading to many possible improvements and new ways to study noise generating mechanisms.

A. CAA simulation

The calculation of the far-field acoustic radiation has been directly achieved by means of a LBM simulation using LABS solver [69], where the LAGOON benchmark is immersed with a 0° yaw angle, in a a low-Mach number subsonic flow ($M = 0.18$). A specific spherical array of radius equal to 13 times one wheel radius and involving 390 virtual microphones (Fig. 3a) has been designed according to a Fibonacci lattice to obtain an even distribution and to completely cover the landing gear. This distribution allows to both optimize the array performances and suitably map the radiated

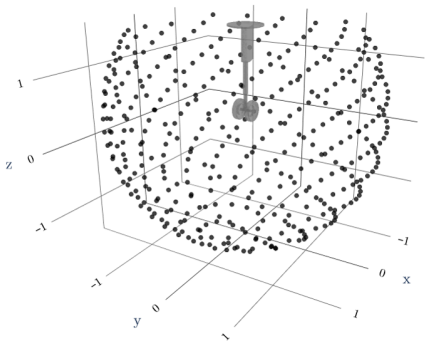

(a) A virtual array of microphones surrounding the LAGOON landing gear.

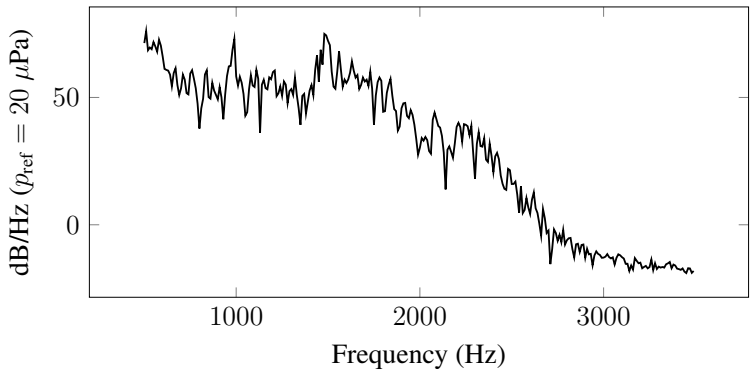

(b) Power Spectral Density at one side microphone.

Figure 3 CAA simulation of a virtual array of microphones.

acoustic field. Each microphone receives simulated time signal of 0.16 s., sampled at 237 717 Hz. Time signals are then processed with a Welch's method [70] to compute the cross-spectral matrix for all frequency bins. The time signals are therefore split into 19 snapshots of 2377 samples and windowed with a Hann function (50 % overlap). Figure 3b represents the Power Spectral Density (PSD) for one microphone and highlights tonal patterns at 1 and 1.5 kHz, as underscored by [71], [68] and [72]. According to Casalino et al. [72], the presence of such periodical fluctuations is due to the coupling of a Rossiter feedback loops [73] inside the wheel rim cavities and acoustic modes between the two wheels. In this interpretation, these frequency peaks are generated by highly and spatially correlated source mechanisms (modal shapes) that may not be clearly localized between the two wheels.

B. 2D acoustic maps

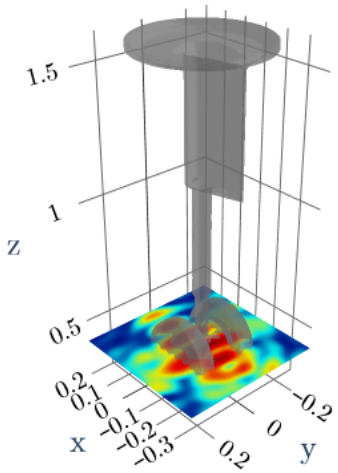

Figure 4 2D Beamforming map with free field monopolar transfer functions, for a frequency $f = 2$ kHz.

Figure 4 shows a typical 2D acoustic map computed for in a xy plane at mid-height of the wheels, with a CBF algorithm and free field monopolar transfer functions, for a frequency $f = 2$ kHz. Multiples lobes can be seen, featuring both the actual acoustic sources and the point spread function of the microphone array. Contrary to most of the literature, where planar arrays were used, the spherical antenna brings alternative array response and acoustic results. Also, 2D maps can be seen as an preliminary step, usually compelled by the planar geometry of microphones arrays, and may not be relevant anymore with 3D spherical antennas.

Figure 5 presents acoustic maps computed with CBF, CLEAN-SC and iterative Bayesian Focusing at the two tonal peaks ($f \in [1, 1.5]$ kHz). These maps can be seen in relation with results computed by Redonnet et al. [71] with a planar array, and show significant discrepancies. While their maps showed that the main source was really concentrated on the axle, Fig. 5 proposes alternate analysis. At $f = 1$ kHz, CBF map (Fig. 5a) indicates the source is mostly located upstream of the axle, which is therefore corroborated by CLEAN-SC (Fig. 5b), while iBF finds also sources outside the wheels (Fig. 5c). At $f = 1.5$ kHz, CBF and iBF (Figs. 5d and 5f) find a particular pattern where the more prominent source is downstream the axle, like the CLEAN-SC result (Fig. 5e). However, multiple precautions must be taken about these results. First, as stated by Casalino et al. [72], the source mechanisms at the origin of these two peaks are mostly modal, defined by a large spatial correlation, which can be delicate to grasp with equivalent sources. Also, the 2D geometry of the calculation grid precludes the use of more advanced but unsuitable transfer functions. Nevertheless, these acoustic maps clearly show that the more prominent source of sound moves from upstream to downstream of the axle between the two frequencies.

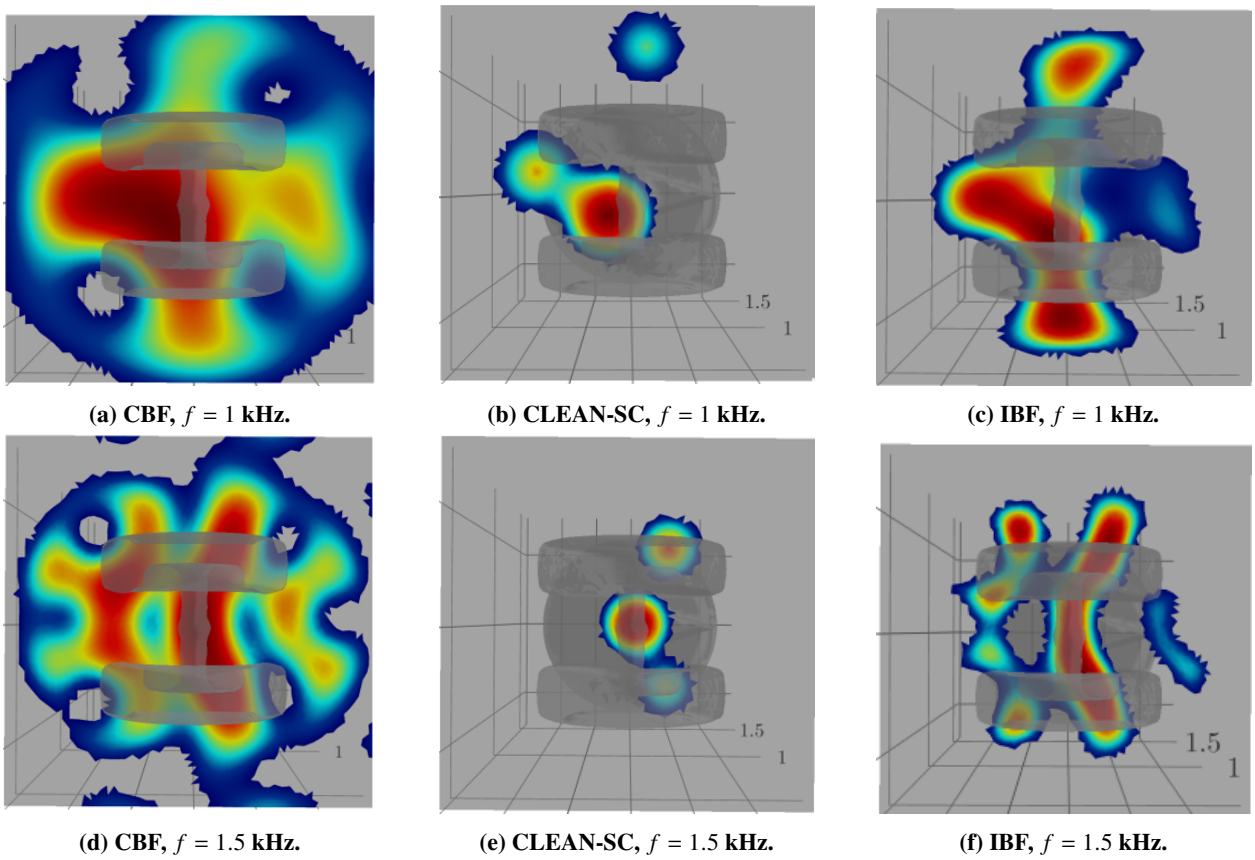

(a) CBF, $f = 1$ kHz. **(b) CLEAN-SC, $f = 1$ kHz.** **(c) IBF, $f = 1$ kHz.**

(d) CBF, $f = 1.5$ kHz. **(e) CLEAN-SC, $f = 1.5$ kHz.** **(f) IBF, $f = 1.5$ kHz.**

Figure 5 2D acoustic maps with various acoustic imaging techniques (CBF, CLEAN-SC and Iterative Bayesian Focusing) for the two tonal peaks $f \in [1, 1.5]$ kHz.

C. 3D localization

As stated above, the use of spherical antennas opens the gate for multiple improvements. The most straightforward is that the entire radiating object can be observed from a large range of angles. Therefore, the mesh of the object (or a decimated version) can be seen as the calculation grid of nodes where potential sources are defined. This modeling implies that aeroacoustic sources are effectively on the skin of the object, which can be inaccurate, if volumetric (quadrupolar) sources are overwhelming the acoustic radiation or if modal sources radiate most of the sound. However, the low Mach number flow of this landing gear simulation may imply that surfacic source distribution can explain a large part of the acoustic radiation. The following figures present 3D acoustic maps computed at two frequencies

corresponding to the first peak (f = 1 kHz) and a non-tonal frequency (f = 2 kHz) to see if radiation patterns differ between the two frequencies, giving insights about the source mechanisms. Hence, four configurations are assessed, with free field monopolar transfer functions and CBF, with free field monopolar and dipolar transfer functions and iBF, and with ESM-based monopolar transfer functions and iBF algorithm.

1. 3D maps at f = 1 kHz

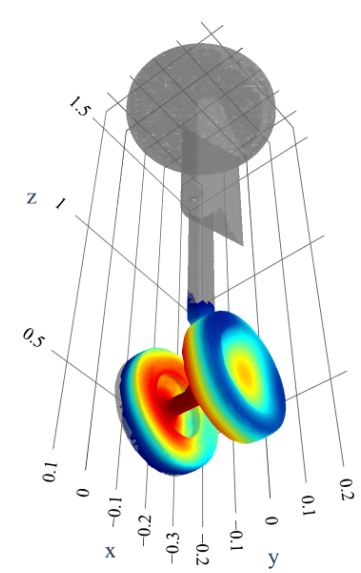

(a) Free field monopolar CBF.

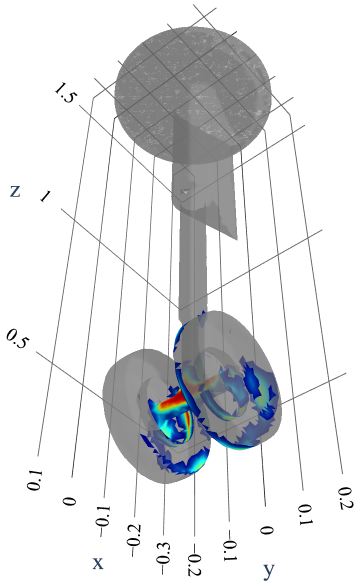

(b) Free field monopolar iBF.

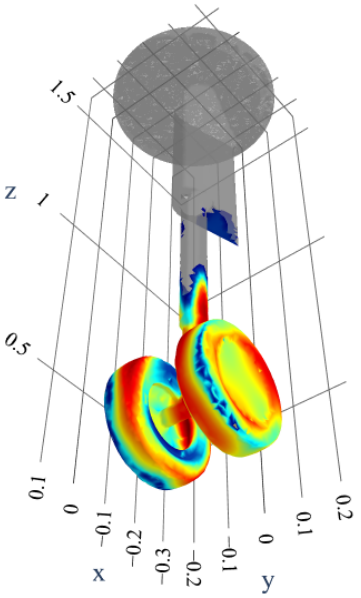

(c) Free field dipolar iBF

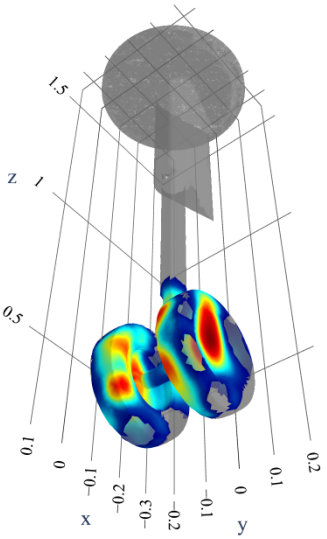

(d) ESM monopolar iBF.

Figure 6 3D acoustic maps computed with various hypotheses, for a frequency f = 1 kHz.

Figure 6 presents results for the tonal frequency f = 1 kHz. Overall, simulations mainly locate the acoustic sources near the wheels, inside their rims or on the axle. A first calculation carried out with a free field monopolar CBF shows a

significant source trace inside the rim and on the axle, mostly upstream of it, as presented in Fig. 5a. The same set-up computed with iBF concentrates the sources upstream of the axle (Fig. 6b, whereas the dipolar version finds sources mainly on the wheels (Fig. 6c). Finally, the ESM-based transfer functions lead to locate the sources both inside the rims and outside the wheels. The variety of results clearly shows that no convergence of analysis is found in this case that may suffer from the modal pattern of the main source. Both CBF and ESM-based transfer function configurations succeed in finding sources inside the rims, but no conclusion can be clearly stated here.

2. 3D maps at $f = 2$ kHz

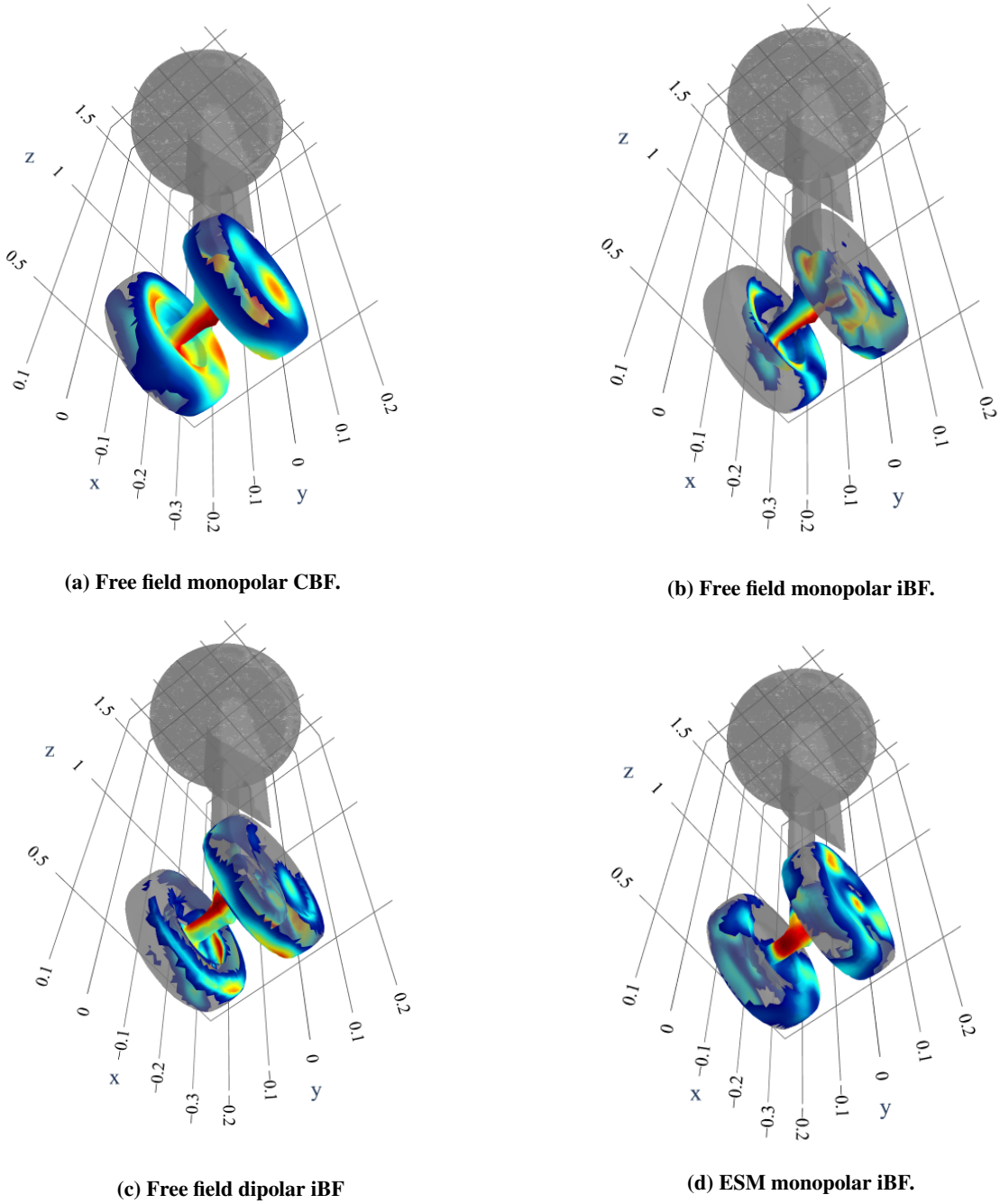

(a) Free field monopolar CBF.

(b) Free field monopolar iBF.

(c) Free field dipolar iBF

(d) ESM monopolar iBF.

Figure 7 3D acoustic maps computed with various hypotheses, for a frequency $f = 2$ kHz.

Figure 7 illustrates the same configurations as above but with a studied frequency $f = 2$ kHz. Here, two major trends emerges. While the free field monopolar computations (CBF (Fig. 7a) and iBF (Fig. 7b)) find the main source downstream of the axle, both the free field dipolar (Fig. 7c) and ESM-based monopolar (Fig. 7d) configurations (both with iBF) locate it upstream of the axle. Contrary to the case at $f = 1$ kHz, couples of results remain consistent according to their leading hypotheses. Hence, the free field monopolar transfer function seems to drive the first results regardless of the acoustic imaging algorithm, which tends to be of secondary importance. On the contrary, free field dipolar and ESM-based transfer functions leads to similar results. This can be explain by the fact that dipoles already contain a part of the diffraction feature, as they are oriented by the mesh normals. Thus the directivity of both source distribution shares similar patterns.

D. Far-field propagation

As seen above, the source localization seems to be significantly affected by the source and propagation models. Therefore, multiple hypotheses can lead to multiple analyses of the same dataset. This section aims at assessing if convergence can be found on the second objective of acoustic imaging, denoted as repropagation (or far-field propagation). Here, the computed source distribution is employed to synthesize the acoustic field around the radiating object.

1. 2D repropagation maps

Figure 8 illustrates the acoustic imaging ability to reproduce the acoustic field radiated by the landing gear. Thus, it highlights the repropagation of the computed equivalent sources at tonal frequencies on lateral and fly-over section planes. As it can be seen, most of the radiated sound seems to be generated by the interaction of the flow and the wheels. Except for Fig. 8c, the following repropagation figures have been computed with iterative Bayesian focusing, as this inverse method can grasp the correlation between equivalent sources, unlike beamforming-like techniques. As explained above, the reconstructed directivity patterns essentially hinge on accurate phase relationships between acoustic sources to correctly synthesize constructive or destructive interferences. Figures 8b and 8d represent bottom views of repropagated acoustic field on the axle median plane at the two tonal peaks ($f = 1$ kHz and $f = 1.5$ kHz). These figures must be assessed in relation with the ones computed by Redonnet et al. [71], especially Figs. 14 and 16. CFD-CAA calculation achieved by Redonnet et al. gave them access to instantaneous pressure field while frequency-formulated acoustic imaging techniques only provide averaged acoustic maps. Casalino et al. [72] and Redonnet et al. demonstrated that the two tonal peaks are generated by Rossiter modes inside the wheel rim cavities and acoustic modes between the two wheels, but the phase interference between these mechanisms produces different radiation patterns, more or less efficient for the two frequencies. At $f = 1$ kHz, the acoustic radiation is driven by an asymmetric pattern, where the wavefront remains mostly in phase in the upstream direction. At $f = 1.5$ kHz, the acoustic field is characterized by one anti-symmetric pattern, where the wave fronts upstream of both sides of the wheels are clearly in opposition of phase. These upstream patterns are well-reconstructed on results presented in Figs. 8. Also, comparisons with maps displayed in [71] show that the silent zones due to destructive interferences well corroborate. This good reconstruction is clearer at $f = 1.5$ kHz, as Redonnet et al. displayed a root mean square map of the pressure field, similar to the result illustrated in Fig. 8d, where the silent zones are well-predicted.

Figures 8c and 8d represent fly-over view of the landing gear radiation at $f = 1.5$ kHz, whose equivalent sources have been computed with CLEAN-SC and iterative Bayesian Focusing, respectively. As explained above, the ability of inverse techniques such as iBF to retrieve correlation between sources is clearly emphasized. CLEAN-SC deals with uncorrelated sources, whose radiation is only the summation of their propagated inner amplitude, revealing a nearly omnidirectional directivity. On Fig. 8c, it is even possible to recognize the three main sources retrieved by CLEAN-SC, as displayed in Fig. 5e. Contrariwise, iBF is able to compute the complete and complex CSM of the sources $\tilde{\mathbf{S}}_{qq}$ and therefore to grasp the interferences between the sources, leading to these multiple silent zones.

2. Far-field spectra

To assess the ability of acoustic imaging techniques to accurately estimate the sound pressure level propagated in the far-field, a set of four receivers has been selected in the virtual microphone array upstream (front position) of the landing gear, under it (bottom position) and at its right and left sides (see Fig. 9). These microphones have not been taken into account to perform acoustic imaging and compute the equivalent sources. The aim of this section is then to retrieve far-field spectra of reference microphones and test the influence of the main three hypotheses of this article : the source

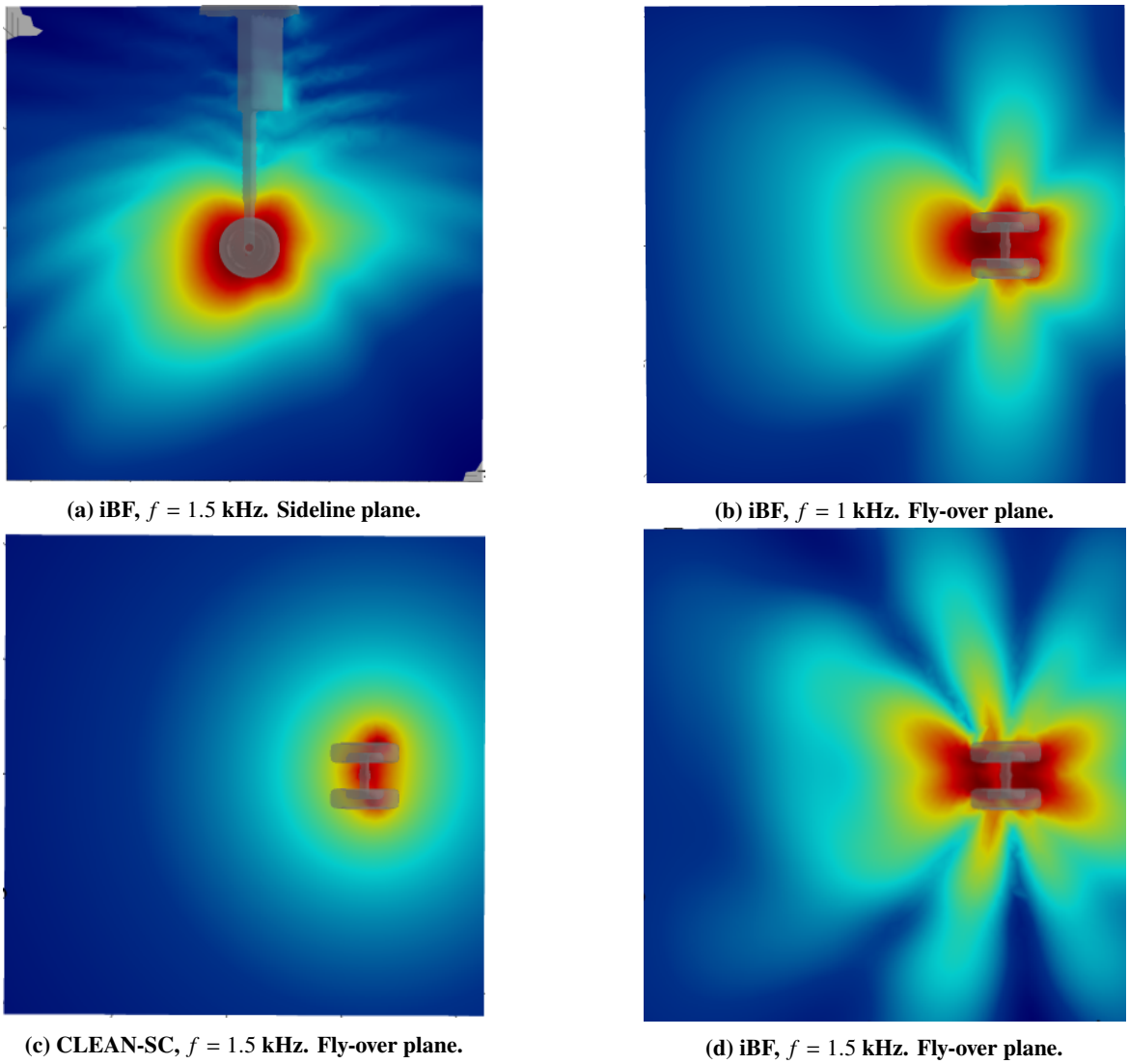

(a) iBF, f = 1.5 kHz. Sideline plane.

(b) iBF, f = 1 kHz. Fly-over plane.

(c) CLEAN-SC, f = 1.5 kHz. Fly-over plane.

(d) iBF, f = 1.5 kHz. Fly-over plane.

Figure 8 Repropagation of equivalent sources in the vicinity of the landing gear. 3D acoustic imaging with free field monopolar transfer functions.

and the propagation model, as well as the inverse method. Figures 10, 11 and 12 present far-field spectra computed for the four receivers with CLEAN-SC and iBF algorithms, considering monopole sources, dipolar sources propagated in free-field condition (Figs. 10-11) and monopolar sources radiated with ESM-based transfer functions (Fig. 12).

The analysis of the far-field spectra reveals that the quality of reconstruction depends on the microphone position, as they can be located near a silent zone where interferences strongly influence the radiation pattern. As primary outcome, these figures highlight the accurate estimations provided by iBF computation. Hence, with a monopolar source distribution assumption (Fig. 10), the two tonal peaks at f = 1 kHz and f = 1.5 kHz are retrieved for the side microphones with iBF, whereas they are not with deconvolution methods. For the bottom microphone (Fig. 10d), while the peak at f = 500 Hz is better reconstructed with CLEAN-SC, the whole spectrum is accurately estimated with inverse methods. The good reconstruction of the peak at f = 500 Hz with CLEAN-SC can also indicate precious information about the source mechanism at its origin in terms of correlation. In a word, iBF succeeds in accurately estimate both the overall sound power levels for an significant frequency range and its multiple peaks, representative of the disturbed directivity of the landing gear.

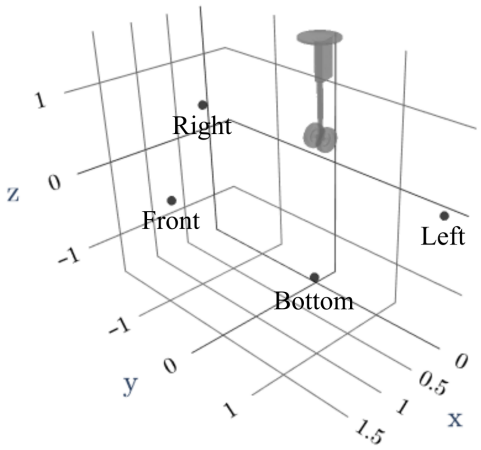

Figure 9 Positions of a set of four virtual receivers considered as references.

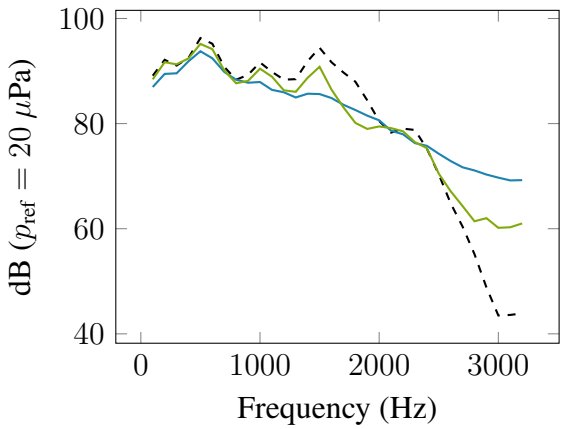

(a) Left microphone.

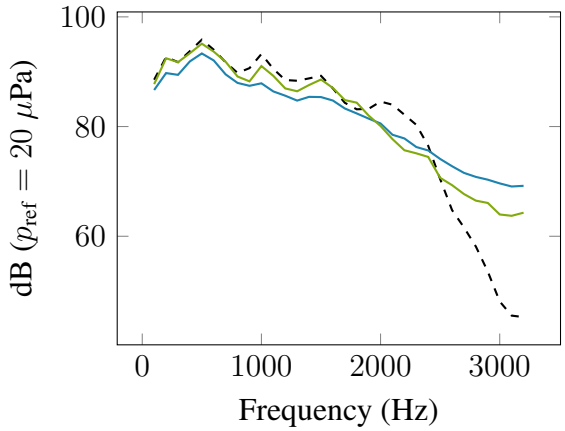

(b) Right microphone.

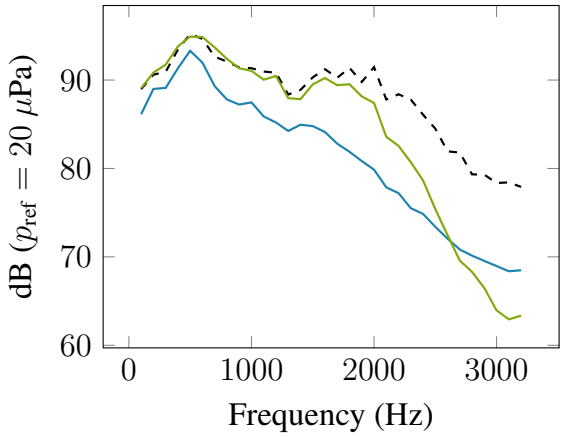

(c) Front microphone.

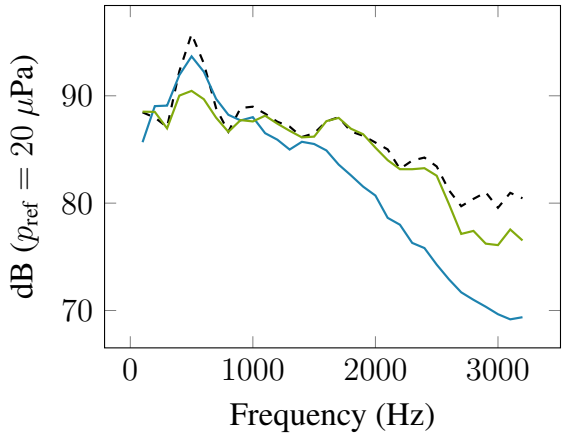

(d) Bottom microphone.

Figure 10 Far-field spectra computed for a selection of four receivers with CLEAN-SC (blue line) and iBF (green line), with a monopolar source hypothesis. The dashed black line represents the reference sound power level estimated from LBM simulation.

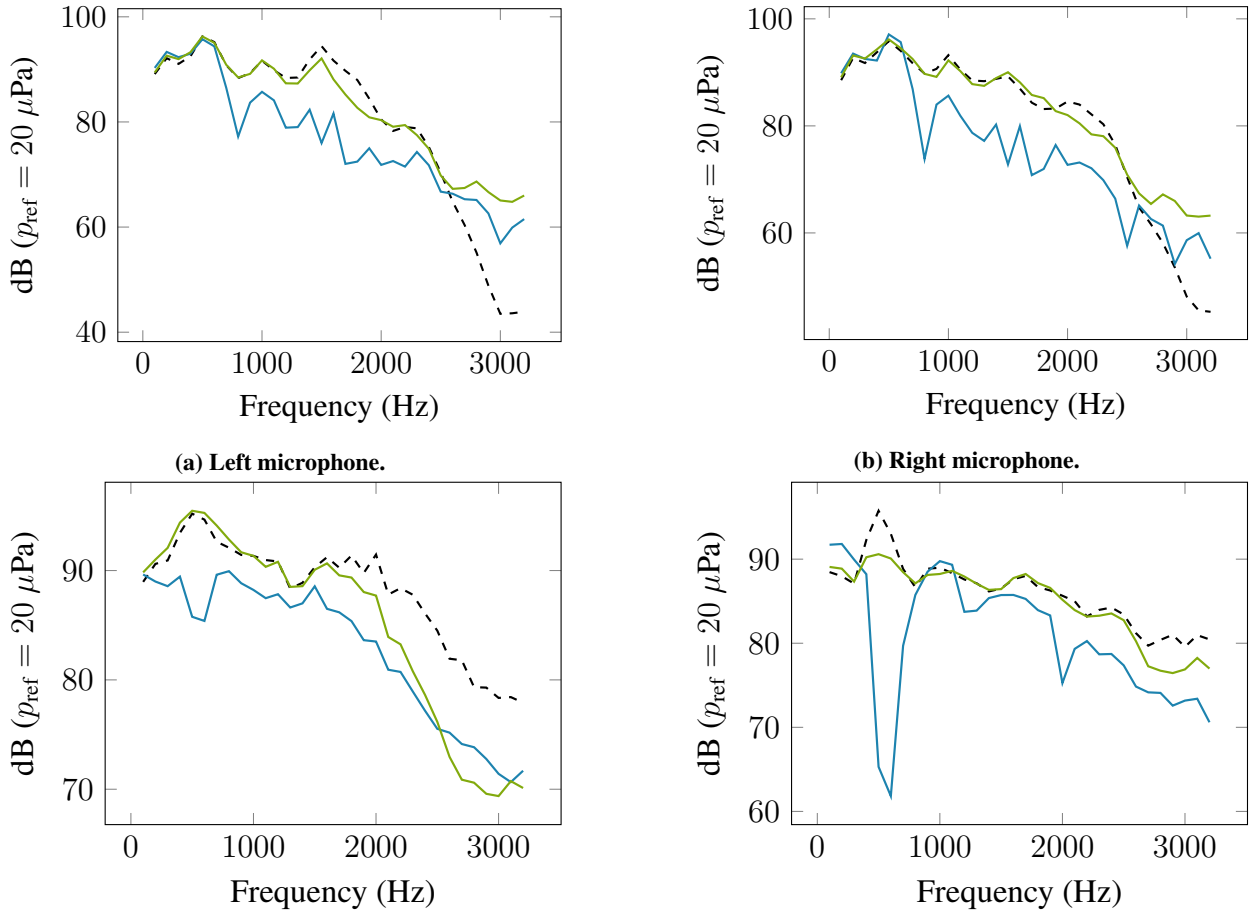

(a) Left microphone.

(b) Right microphone.

(c) Front microphone.

(d) Bottom microphone.

Figure 11 Far-field spectra computed for a selection of four receivers with CLEAN-SC (blue line) and iBF (green line), with a dipolar source hypothesis. The dashed black line represents the reference sound power level estimated from LBM simulation.

Figure 11 displays the same results with a dipolar source distribution hypothesis. It can be seen that the iBF performances are slightly improved for the side microphones (Figs. 11a and 11b), while the gain is less visible than for the others microphones. However, the far-field spectra computed with a deconvolution method are heavily disturbed by the dipolar source model. Again, the correlation between the source is here a decisive factor, as dipolar sources are highly directional. The least error of source combination can lead to massive errors due to interference patterns. As stated by several authors, dipolar models are sensitive and arduous to finely tune. However, iBF manages to cope with alternative source models.

Finally, Fig. 12 presents far-field spectra computed with ESM-based transfer functions and a monopolar source distribution. For this specific configuration, the ESM-based transfer functions clearly do not improve the acoustic field reconstruction at the four receivers positions. The deconvoluted results are slightly modified for side microphones while they are severely disturbed at the front and bottom positions. For its part, iBF-based far-field spectra are not significantly altered by the transfer functions influence, even if no gain of performances is observed.

The presented results bring out the balance between the three main hypotheses of this article. First, the choice of the array processing algorithm is of utmost importance. All figures point out the relevancy of inverse methods such as iterative Bayesian Focusing to reproduce the radiated acoustic field and quantitatively estimate the far-field spectra received by virtual microphones. The accurate prediction of source correlation greatly influences the directivity of the

equivalent sources, and only inverse methods is able to grasp such mechanisms. The choice of the source distribution comes in second place. Slight improvement is observed with dipolar equivalent sources, which can more precisely reproduce the directivity of the aeroacoustic sources on the radiating object. As an additional feature, dipolar source can also catch a part of the diffraction effect, as the radiation of the dipoles is driven by their mesh normals. Therefore, the combination of the directivity and the correlation of the estimated dipolar distribution may clutch the more prominant patterns of the diffraction effects. Finally, the results proposed with a monopolar source distribution hypothesis and ESM-based transfer functions show no particular gain of efficiency compared with the previous ones, as explained above. It should also be noted that the particular shape of the landing gear, the frequency range and its size are less prone to diffraction effects than larger object such as cars or aircraft frame, and masking effects induced by the presence of the radiating object itself on the path that lies between mesh cells and virtual microphones are therefore less significant.

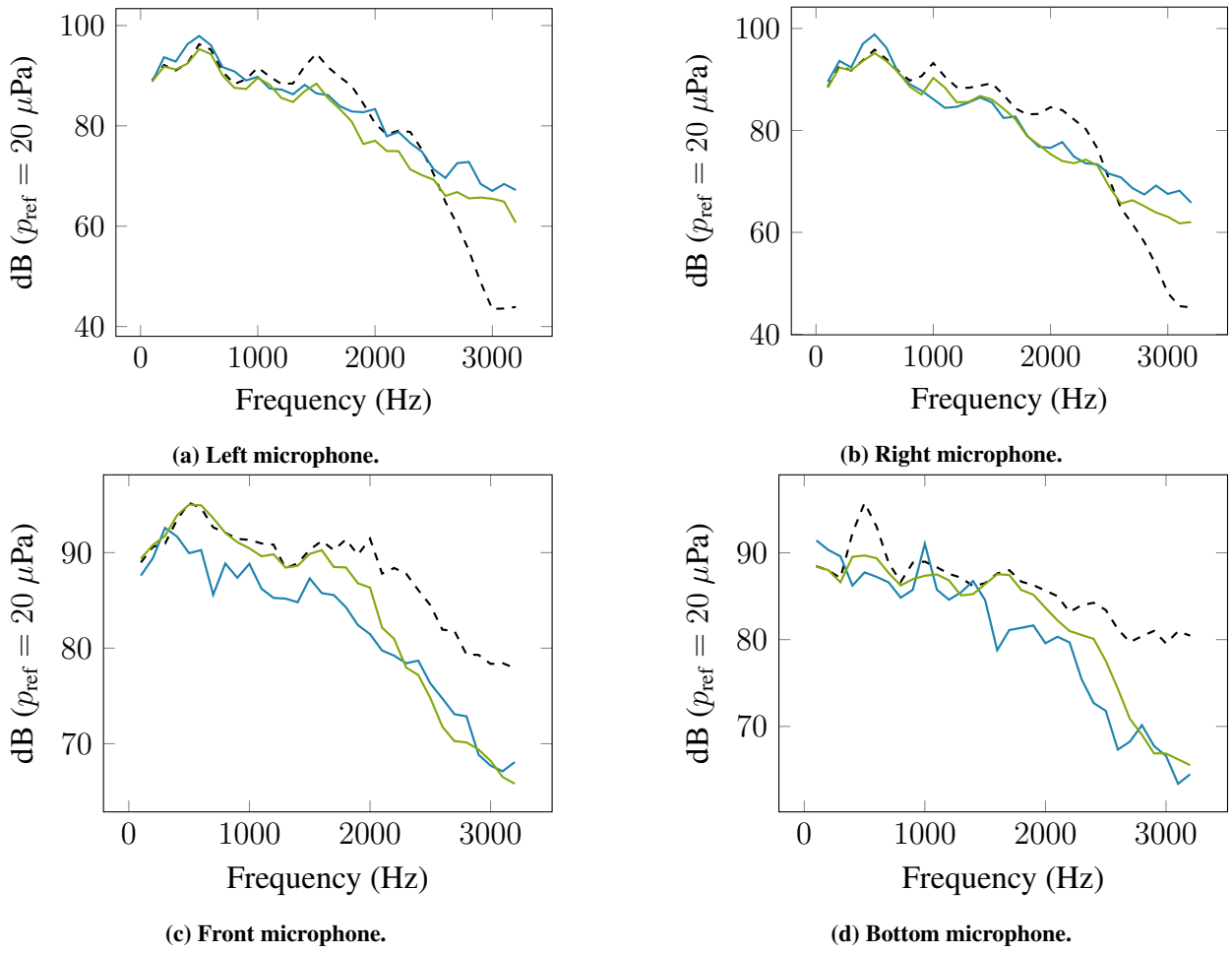

(a) Left microphone.

(b) Right microphone.

(c) Front microphone.

(d) Bottom microphone.

Figure 12 Far-field spectra computed for a selection of four receivers with CLEAN-SC (blue line) and iBF (green line), with a monopolar source distribution hypothesis and ESM-based transfer functions. The dashed black line represents the reference sound power level estimated from LBM simulation.

VII. Conclusion

Acoustic imaging techniques are widely employed in experimental campaigns to both localize acoustic hot spots and estimate their sound power levels. In recent years, authors of the aeroacoustic community began to apply these methods to CAA data computed on virtual arrays of microphones surrounding radiating objects immersed in flows and showed their promising prospects. A great deal of effort has been made to develop reliable connections between CAA simulations and array processing techniques. However, almost all studied configurations made use of two-dimensional

conventional beamforming, sometimes improved by an additional deconvolution step, considering as calculation grid an uncorrelated distribution of monopolar sources with free field transfer functions. On this basis, this paper draws a first attempt at enhancing CAA-based acoustic imaging involving advanced hypotheses and methods, suited to three-dimensional aeroacoustic applications. Hence, the dipolar nature of surfacic aeroacoustic sources is modeled, as well as the diffracting transfer functions due to the presence of the radiating object on the path between sources and receivers. Furthermore, the source correlation is retrieved with the help of inverse method such as iterative Bayesian Focusing. These improvements are assessed against the LAGOON landing gear benchmark. This evaluation is twofold : first, the ability to localize source distribution on the object mesh is studied at some tonal and non-tonal frequencies. At the first peak, it seems clear that the modal pattern of the source mechanism puts the acoustic imaging to the test as the underlying process at the core of the technique is may not be well-suited to this configuration. As a result, various conclusions can be drawn about the true localization of the sources, whose spatial correlation may locate them everywhere in the volume between the wheels. At the non-tonal frequency, the sources are more precisely located on the axle, upstream or downstream it according to the source modeling. These multiples analyses should lead us to pursue our investigation on this track to more finely understand the genuine source mechanisms. Second, the problem of the far-field propagation of the determined potential sources (or repropagation) is examined, where it clearly shows that inverse methods are mandatory to accurately reconstruct the acoustic radiation. Indeed, the correlation between the sources acts as a crucial factor in the far-field directivity. In this regard, iterative Bayesian Focusing proves its ability to reconstruct complex spatial patterns and accurately estimates far-field spectra. In this configuration, other hypotheses as the dipolar nature of the sources or diffraction effects seem of secondary importance.

Acknowledgments

This work was partially performed in the framework of the CALM-AA project, funded by Région Auvergne Rhône-Alpes (AURA), BPI France and the European Union through the European Regional Fund (FEDER). The authors also thank Emmanuel Julliard from Airbus Operations S.A.S for providing us data from LBM simulation.

References

[1] Riegel, M., Blumrich, R., Oettle, N., Harriet, V., Minck, O., and Verrecas, B., "New Large Microphone Array at the FKFS Wind Tunnel," *12th FKFS Conference: Progress in Vehicle Aerodynamics and Thermal Management*, 2019.

[2] Lockard, D. P., Humphreys, W. M., Khorrami, M. R., Fares, E., Casalino, D., and Ravetta, P. A., "Comparison of computational and experimental microphone array results for an 18% scale aircraft model," *International journal of aeroacoustics*, Vol. 16, No. 4-5, 2017, pp. 358–381.

[3] Pignier, N. J., O'Reilly, C. J., and Boij, S., "Identifying equivalent sound sources from aeroacoustic simulations using a numerical phased array," *Journal of Sound and Vibration*, Vol. 394, 2017, pp. 203–219.

[4] Antoni, J., Le Magueresse, T., Leclère, Q., and Simard, P., "Sparse acoustical holography from iterated Bayesian focusing," *Journal of Sound and Vibration*, Vol. 446, 2019, pp. 289–325.

[5] Battista, G., Chiariotti, P., Martarelli, M., and Castellini, P., "Inverse methods in aeroacoustic three-dimensional volumetric noise source localization and quantification," *Journal of Sound and Vibration*, Vol. 473, 2020, p. 115208.

[6] Zamponi, R., Chiariotti, P., Battista, G., Schram, C., and Castellini, P., "3D Generalized Inverse Beamforming in wind tunnel aeroacoustic testing: application to a Counter Rotating Open Rotor aircraft model," *Applied Acoustics*, Vol. 163, 2020, p. 107229.

[7] Zhou, Y., Valeau, V., Marchal, J., Ollivier, F., and Marchiano, R., "Three-dimensional identification of flow-induced noise sources with a tunnel-shaped array of MEMS microphones," *Journal of Sound and Vibration*, Vol. 482, 2020, p. 115459.

[8] Liu, Y., Quayle, A. R., Dowling, A. P., and Sijtsma, P., "Beamforming correction for dipole measurement using two-dimensional microphone arrays," *The Journal of the Acoustical Society of America*, Vol. 124, No. 1, 2008, pp. 182–191.

[9] Porteous, R., Prime, Z., Doolan, C. J., Moreau, D. J., and Valeau, V., "Three-dimensional beamforming of dipolar aeroacoustic sources," *Journal of Sound and Vibration*, Vol. 355, 2015, pp. 117–134.

[10] Evans, D., Hartmann, M., and Delfs, J., "Beamforming for point force surface sources in numerical data," *Journal of Sound and Vibration*, Vol. 458, 2019, pp. 303–319.

[11] Gao, J., Wu, H., and Jiang, W., "Dipole-based beamforming method for locating dipole sources with unknown orientations in three-dimensional domains," *The Journal of the Acoustical Society of America*, Vol. 147, No. 1, 2020, pp. 125–136.

[12] Chambon, J., Minck, O., Bouley, S., and Antoni, J., "Dipolar-base equivalent sources method for three-dimensional aeroacoustic source identification," *9th Berlin Beamforming Conference (BeBeC 2022)*, 2022.

[13] Chambon, J., Antoni, J., and Bouley, S., "Galerkin equivalent sources method for sound field reconstruction around diffracting bodies," *The Journal of the Acoustical Society of America*, Vol. 152, No. 4, 2022, pp. 2042–2053.

[14] Ffowcs Williams, J. E., and Hawkings, D. L., "Sound generation by turbulence and surfaces in arbitrary motion," *Philosophical Transactions for the Royal Society of London. Series A, Mathematical and Physical Sciences*, 1969, pp. 321–342.

[15] Du, Y., and Morris, P., "Numerical investigation of the noise source locations of supersonic jets using the beamformed method," *50th AIAA Aerospace Sciences Meeting including the New Horizons Forum and Aerospace Exposition*, 2012, p. 1169.

[16] Panickar, P., Sinha, N., and Murray, N., "Localization of acoustic sources in shock-containing jet flows using phased array measurements," *51st AIAA Aerospace Sciences Meeting including the New Horizons Forum and Aerospace Exposition*, 2013, p. 613.

[17] Armstrong, D., Najafi-Yazdi, A., Mongeau, L. G., and Raymond, V., "Numerical simulations of flow over a landing gear with noise reduction devices using the lattice-boltzmann method," *19th AIAA/CEAS Aeroacoustics Conference*, 2013, p. 2114.

[18] Erwin, J. P., Panickar, P., Vogel, P., and Sinha, N., "Acoustic source localization of rectangular jets using large eddy simulation with numerical phased arrays," *52nd Aerospace Sciences Meeting*, 2014, p. 0179.

[19] Nelson, C. C., Cain, A. B., Dougherty, R., Brentner, K. S., and Morris, P. J., "Application of synthetic array techniques for improved simulations of hot supersonic jet noise," *International Journal of Aeroacoustics*, Vol. 16, No. 4-5, 2017, pp. 382–402.

[20] Du, Y., and Morris, P. J., "The separation of radiating and non-radiating near-field pressure fluctuations in supersonic jets," *Journal of Sound and Vibration*, Vol. 355, 2015, pp. 172–187.

[21] Fleury, V., and Davy, R., "Analysis of jet–airfoil interaction noise sources by using a microphone array technique," *Journal of Sound and Vibration*, Vol. 364, 2016, pp. 44–66.

[22] Brooks, T. F., and Humphreys, W. M., "A deconvolution approach for the mapping of acoustic sources (DAMAS) determined from phased microphone arrays," *Journal of sound and vibration*, Vol. 294, No. 4-5, 2006, pp. 856–879.

[23] Sijtsma, P., "CLEAN based on spatial source coherence," *International journal of aeroacoustics*, Vol. 6, No. 4, 2007, pp. 357–374.

[24] Brusniak, L., Shur, M., and Spalart, P., "Phased-array imaging of jet noise sources in a large-eddy simulation," *12th AIAA/CEAS Aeroacoustics Conference (27th AIAA Aeroacoustics Conference)*, 2006, p. 2444.

[25] Adam, J.-L., Menoret, A., and Ricot, D., "Direct aeroacoustic source identification based on lattice boltzmann simulation and beamforming technique," *15th AIAA/CEAS Aeroacoustics Conference (30th AIAA Aeroacoustics Conference)*, 2009, p. 3182.

[26] Dougherty, R. P., Ramachandran, R. C., and Raman, G., "Deconvolution of sources in aeroacoustic images from phased microphone arrays using linear programming," *International Journal of Aeroacoustics*, Vol. 12, No. 7-8, 2013, pp. 699–717.

[27] Curle, N., "The influence of solid boundaries upon aerodynamic sound," *Proceedings of the Royal Society of London. Series A. Mathematical and Physical Sciences*, Vol. 231, No. 1187, 1955, pp. 505–514.

[28] Brentner, K. S., and Farassat, F., "Analytical comparison of the acoustic analogy and Kirchhoff formulation for moving surfaces," *AIAA journal*, Vol. 36, No. 8, 1998, pp. 1379–1386.

[29] Ewert, R., and Schröder, W., "Acoustic perturbation equations based on flow decomposition via source filtering," *Journal of Computational Physics*, Vol. 188, No. 2, 2003, pp. 365–398.

[30] Chen, S., and Doolen, G. D., "Lattice Boltzmann method for fluid flows," *Annual review of fluid mechanics*, Vol. 30, No. 1, 1998, pp. 329–364.

[31] Brentner, K. S., and Farassat, F., "Modeling aerodynamically generated sound of helicopter rotors," *Progress in aerospace sciences*, Vol. 39, No. 2-3, 2003, pp. 83–120.

[32] Isom, M. P., "The theory of sound radiated by a hovering transonic helicopter blade," *Poly-AE/AM*, Vol. 75, No. 4, 1975.

[33] Farassat, F., "The derivation of a thickness noise formula for the far-field by Isom," *Journal of Sound Vibration*, Vol. 64, No. 1, 1979, pp. 159–160.

[34] Farassat, F., "Extension of Isom's thickness noise formula to the near field," *Journal of Sound Vibration*, Vol. 67, No. 2, 1979, pp. 280–281.

[35] Chu, B.-T., and Kovásznay, L. S., "Non-linear interactions in a viscous heat-conducting compressible gas," *Journal of Fluid Mechanics*, Vol. 3, No. 5, 1958, pp. 494–514.

[36] Hajczak, A., Sanders, L., Vuillot, F., and Druault, P., "A comparison between off and on-body control surfaces for the FW-H equation: Application to a non-compact landing gear wheel," *Journal of Sound and Vibration*, Vol. 490, 2021, p. 115730.

[37] Farassat, F., "Theory of noise generation from moving bodies with an application to helicopter rotors," Tech. Rep. Tech. Rep. R-451, NASA, Langley Research Center, 1975.

[38] Farassat, F., "Derivation of Formulations 1 and 1A of Farassat," Tech. Rep. Technical Report NASA/TM-2007-214853, L-19318, NASA, Langley Research Center, 2007.

[39] Weckmüller, C., Wellner, J., Guerin, S., and Michel, U., "Ffowcs Williams & Hawkings formulation for the convective wave equation and permeable data surface," *16th AIAA/CEAS Aeroacoustics Conference*, 2010, p. 3710.

[40] Wells, V., and Han, A., "Acoustics of a moving source in a moving medium with application to propeller noise," *Journal of sound and vibration*, Vol. 184, No. 4, 1995, pp. 651–663.

[41] Najafi-Yazdi, A., Brès, G. A., and Mongeau, L., "An acoustic analogy formulation for moving sources in uniformly moving media," *Proceedings of the Royal Society A: Mathematical, Physical and Engineering Sciences*, Vol. 467, No. 2125, 2011, pp. 144–165.

[42] Sarradj, E., "Three-dimensional acoustic source mapping with different beamforming steering vector formulations," *Advances in Acoustics and Vibration*, Vol. 2012, 2012.

[43] Chardon, G., "Theoretical analysis of beamforming steering vector formulations for acoustic source localization," *Journal of Sound and Vibration*, Vol. 517, 2022, p. 116544.

[44] Jordan, P., Fitzpatrick, J. A., and Valiere, J.-C., "Measurement of an aeroacoustic dipole using a linear microphone array," *The Journal of the Acoustical Society of America*, Vol. 111, No. 3, 2002, pp. 1267–1273.

[45] Holland, K., and Nelson, P., "An experimental comparison of the focused beamformer and the inverse method for the characterisation of acoustic sources in ideal and non-ideal acoustic environments," *Journal of Sound and Vibration*, Vol. 331, No. 20, 2012, pp. 4425–4437.

[46] Lee, S., "The use of equivalent source method in computational acoustics," *Journal of Computational Acoustics*, Vol. 25, No. 01, 2017, p. 1630001.

[47] Dunn, M., and Tinetti, A., "Aeroacoustic scattering via the equivalent source method," *10th AIAA/CEAS Aeroacoustics Conference*, 2004, p. 2937.

[48] Le Magueresse, T., "Approche unifiée multidimensionnelle du problème d'identification acoustique inverse," Ph.D. thesis, Lyon, 2016.

[49] Minck, O., Le Magueresse, T., Lamotte, L., Locqueteau, C., and Bouvet, P., "Array based acoustic power measurement, Renault pass-by noise," *FISITA World Automotive Congress, Busan, Korea*, 2016.

[50] Samarasinghe, P., Abhayapala, T. D., and Kellermann, W., "Acoustic reciprocity: An extension to spherical harmonics domain," *The Journal of the Acoustical Society of America*, Vol. 142, No. 4, 2017, pp. EL337–EL343.

[51] Rayleigh, J. W. S. B., *The theory of sound*, Vol. 2, Macmillan & Company, 1896.

[52] Chambon, J., Le Magueresse, T., Minck, O., and Antoni, J., "Three-dimensional beamforming for wind tunnel applications using ESM-based transfer functions," *Berlin Beamforming Conference*, 2020.

[53] Koopmann, G. H., Song, L., and Fahnline, J. B., "A method for computing acoustic fields based on the principle of wave superposition," *The Journal of the Acoustical Society of America*, Vol. 86, No. 6, 1989, pp. 2433–2438.

[54] Amiet, R., "Refraction of sound by a shear layer," *Journal of Sound and Vibration*, Vol. 58, No. 4, 1978, pp. 467–482.

[55] Leclère, Q., Pereira, A., Bailly, C., Antoni, J., and Picard, C., "A unified formalism for acoustic imaging based on microphone array measurements," *International Journal of Aeroacoustics*, Vol. 16, No. 4-5, 2017, pp. 431–456.

[56] Merino-Martínez, R., Sijtsma, P., Snellen, M., Ahlefeldt, T., Antoni, J., Bahr, C. J., Blacodon, D., Ernst, D., Finez, A., Funke, S., et al., "A review of acoustic imaging methods using phased microphone arrays," *CEAS Aeronautical Journal*, Vol. 10, No. 1, 2019, pp. 197–230.

[57] Elias, G., "Experimental techniques for source location," *Lectures Series 1997–07 Aeroacoustics and Active Noise Control*, 1997.

[58] Antoni, J., "A Bayesian approach to sound source reconstruction: Optimal basis, regularization, and focusing," *The Journal of the Acoustical Society of America*, Vol. 131, No. 4, 2012, pp. 2873–2890.

[59] Sijtsma, P., Merino-Martinez, R., Malgoezar, A. M., and Snellen, M., "High-resolution CLEAN-SC: Theory and experimental validation," *International Journal of Aeroacoustics*, Vol. 16, No. 4-5, 2017, pp. 274–298.

[60] Hadamard, J., "Sur les problèmes aux dérivées partielles et leur signification physique," *Princeton university bulletin*, 1902, pp. 49–52.

[61] Tikhonov, A. N., Goncharsky, A., Stepanov, V. V., and Yagola, A. G., *Numerical methods for the solution of ill-posed problems*, Vol. 328, Springer Science & Business Media, 1995.

[62] Golub, G. H., Heath, M., and Wahba, G., "Generalized cross-validation as a method for choosing a good ridge parameter," *Technometrics*, Vol. 21, No. 2, 1979, pp. 215–223.

[63] Hansen, P. C., *Rank-deficient and discrete ill-posed problems: numerical aspects of linear inversion*, SIAM, 1998.

[64] Pereira, A., Antoni, J., and Leclère, Q., "Empirical Bayesian regularization of the inverse acoustic problem," *Applied Acoustics*, Vol. 97, 2015, pp. 11–29.

[65] Bouchouireb, H., Pignier, N. J., Dahan, J. A., O'Reilly, C. J., and Boij, S., "Identification of noise sources on a realistic landing gear using numerical phased array methods applied to computational data," *23rd AIAA/CEAS Aeroacoustics Conference*, 2017, p. 3019.

[66] Rougier, T., Bouvy, Q., Casalino, D., Appelbaum, J., and Kleinclaus, C., "Design of quieter landing gears through lattice-Boltzmann CFD simulations," *21st AIAA/CEAS Aeroacoustics Conference*, 2015, p. 3259.

[67] Manoha, E., and Caruelle, B., "Summary of the LAGOON solutions from the Benchmark problems for Airframe Noise Computations-III Workshop," *21st AIAA/CEAS aeroacoustics conference*, 2015, p. 2846.

[68] Bulté, J., and Redonnet, S., "Landing gear noise identification using phased array with experimental and computational data," *AIAA Journal*, Vol. 55, No. 11, 2017, pp. 3839–3850.

[69] Sengissen, A., Giret, J.-C., Coreixas, C., and Boussuge, J.-F., "Simulations of LAGOON landing-gear noise using lattice Boltzmann solver," *21st AIAA/CEAS aeroacoustics conference*, 2015, p. 2993.

[70] Welch, P., "The use of fast Fourier transform for the estimation of power spectra: a method based on time averaging over short, modified periodograms," *IEEE Transactions on audio and electroacoustics*, Vol. 15, No. 2, 1967, pp. 70–73.

[71] Redonnet, S., Khelil, S. B., Bulté, J., and Cunha, G., "Numerical characterization of landing gear aeroacoustics using advanced simulation and analysis techniques," *Journal of Sound and Vibration*, Vol. 403, 2017, pp. 214–233.

[72] Casalino, D., Ribeiro, A. F., Fares, E., and Nölting, S., "Lattice–Boltzmann aeroacoustic analysis of the LAGOON landing-gear configuration," *AIAA journal*, Vol. 52, No. 6, 2014, pp. 1232–1248.

[73] Rossiter, J., "Wind-tunnel experiments on the flow over rectangular cavities at subsonic and transonic speeds," Tech. Rep. Report No. 3438, Aeronautical Research Council, 1964.